PEGylated Polypyrrole Nanoparticles Conjugating Gadolinium Chelates for Dual-Modal MRI/Photoacoustic Imaging Guided Photothermal Therapy of Cancer

Xiaolong Liang, Yanyan Li, Xiaoda Li, Lijia Jing, Zijian Deng, Xiuli Yue, Changhui Li, and Zhifei Dai**

Polypyrrole nanoparticles conjugating gadolinium chelates were successfully fabricated for dual-modal magnetic resonance imaging (MRI) and photoacoustic imaging guided photothermal therapy of cancer, from a mixture of pyrrole and pyrrole-1-propanoic acid through a facile one-step aqueous dispersion polymerization, followed by covalent attachment of gadolinium chelate, using polyethylene glycol as a linker. The obtained PEGylated polypyrrole nanoparticles conjugating gadolinium chelates (Gd-PEG-PPy NPs), sized around around 70 nm, exhibited a high T_1 relaxivity coefficient of 10.61 L mM^{-1} s^{-1}, more than twice as high as that of the relating free Gd^{3+} complex (4.2 L mM^{-1} s^{-1}). After 24 h intravenous injection of Gd-PEG-PPy NPs, the tumor sites exhibited obvious enhancement in both T_1-weighted MRI intensity and photoacoustic signal compared with that before injection, indicating the efficient accumulation of Gd-PEG-PPy NPs due to the introduction of the PEG layer onto the particle surface. In addition, tumor growth could be effectively inhibited after treatment with Gd-PEG-PPy NPs in combination with near-infrared laser irradiation. The passive targeting and high MRI/photoacoustic contrast capability of Gd-PEG-PPy NPs are quite favorable for precise cancer diagnosing and locating the tumor site to guide the external laser irradiation for photothermal ablation of tumors without damaging the surrounding healthy tissues. Therefore, Gd-PEG-PPy NPs may assist in better monitoring the therapeutic process, and contribute to developing more effective "personalized medicine," showing great potential for cancer diagnosis and therapy.

1. Introduction

Photothermal therapy (PTT) using photothermal agents in combination of near infrared (NIR) light has gained increasing attention in recent years as a minimally invasive approaches for cancer treatment because it involves delivery of high thermal energy to cancer tissue with little collateral damage to the normal tissue.[1–5] However, for effective, safe and personalized PTT treatment, it is crucial to identify the location and size of the tumors before therapy, to monitor the in vivo distribution of photothermal agents during therapy and evaluate effectiveness after therapy with appropriate imaging techniques.[6–8] So theranostic agents with functions of both imaging, diagnosis, and therapy have attracted intensive research interests, allowing for therapeutic feedback through monitoring the status of injected agents and instantaneous responses to treatment.[9–14] In addition, the use of theranostic agents can avoid administration of multiple doses of agents, hence reduce greatly putting additional stress on the body's blood clearance.

Magnetic resonance imaging (MRI) is one of the most reliable diagnostic tools due to its capability to provide 3D topographical data and timely feedback information of disease tissue in vivo.[15–18] However, conventional clinical MRI systems can present merely a structure of soft tissues and bone marrow with a typical resolution to ca. 0.5 mm, which is not enough to identify microstructures and boundary of lesions.[19,20] With the aid of the contrast agents, MRI can provide more detailed anatomical information with high quality and sensitivity and achieve molecular imaging. Iron oxide nanoparticles (NPs) are the first clinically used T_2 contrast agent,[21] but the induced negative contrast may be confused with areas of innate hypointensities.[22] In contrast, T_1 contrast agents of Gd^{3+} complexes have been the predominant in clinical MR imaging due to their high contrast capability without disruption of magnetic homogeneity.[23–27] Compared with MRI, photoacoustic imaging (PAI) is a new emerging hybrid imaging modality based on the measurement of ultrasonic waves induced by biological tissues' absorption of short laser pulses.[28] In combination of spectral selectivity of laser light and high resolution of ultrasound detection, PAI has proven to be a promising technique

Dr. X. Liang, Dr. Z. Deng, Prof. C. Li, Prof. Z. Dai
Department of Biomedical Engneering
College of Engineering
Peking University
Beijing 100871, P.R. China
E-mail: xiaolong.liang@moon.ibp.ac.cn;
zhifei.dai@pku.edu.cn
Dr. Y. Li, Dr. X. Li, Dr. L. Jing, Prof. X. Yue
Nanomedicine and Biosensor Laboratory
School of Life Science and Technology
Harbin Institute of Technology
Harbin 150080, P.R. China

DOI: 10.1002/adfm.201402338

for visualizing tissue structures and functions with high contrast at unprecedented depth.[29–31] However, a single-modality imaging technique usually provide insufficient information for diagnosis. Considering each imaging modality possesses its own advantages and limitations, multiple-modality imaging has drawn extensive attention in biomedical research recently because of its ability to provide more comprehensive information for accurate diagnosis.[19,32,33] Therefore, it is undoubted that the combination of magnetic resonance (MR) and photoacoustic (PA) imaging would conduce to accurate locating of cancerous tissue for more precise guidance of PTT. MRI can rapidly screen to locate the potential lesions, while PAI can provide high-resolution morphological structure and molecular information in highly sensitivity. As a result, a probe with properties of both strong magnetization and light absorption can serve as an excellent contrast agent when used for the dual MR/PA imaging.

Currently, a large number of materials with strong optical NIR absorption have been explored as photothermal agents for PTT.[34–54] In the past decade, PTT nanoagents were mainly focused on inorganic nanomaterials, such as gold nanomaterials (Au nanoshells, nanorods, and nanocages),[34–38] carbon nanomaterials (carbon nanotube and graphene),[39–41] copper sulfide nanoparticles,[42–44] and so on. Very recently, NIR-absorbing conjugated polymers, such as polyaniline, poly(3,4-ethylenedioxythiophene)poly(styrenesulfonate) (PEDOT:PSS) and polypyrrole (PPy) have been reported to act as photothermal agents, showing promising cancer ablation effect both in vitro and in vivo.[45–51] Among all these NIR absorbing nanomaterials, uniform PPy NPs are of particular importance as a novel promising photothermal agent for localized tumorous PTT because of their good in vitro and in vivo biocompatibility, significant photothermal conversion efficiency, and remarkable photostability.[52,53] In addition, it has been demonstrated that PPy NPs show great potential to be used as a new polymer-based nanoparticulate optical contrast agent to enhance PA imaging due to strong absorbance in the NIR region.[54]

This paper reports the fabrication of PEGylated polypyrrole nanoparticles conjugating gadolinium chelates (Gd-PEG-PPy NPs) for dual-modal MRI/photoacoustic imaging guided photothermal therapy of cancer from the mixture of pyrrole (Py) and pyrrole-1-propanoic acid (COOH-Py) with different molar ratios through microemulsion method, followed by covalent attachment of gadolinium chelate (Gd-DOTA) using polyethylene glycol (PEG)-bis-amine as bridge (**Scheme 1**). The introduction of the PEG spacer endows the nanoparticle with good water-solubility and physiological stability, greatly prolonging the blood circulation time. Both in vitro and in vivo experiments indicated that Gd-PEG-PPy NPs showed good biocompatibility and excellent performance for imaging guided photothermal therapy. Although the Gd-PEG-PPy NPs presented here may not work for all sorts of cancers, it provides a promising multifunctional nanoplatform for further conjugation with targeting moieties and achieving specific cancer theranostics.

2. Results and Discussion

2.1. Preparation and Characterization of Gd-PEG-PPy NPs

The COOH-PPy NPs were synthesized via a facile one-step aqueous dispersion polymerization using polyvinyl alcohol (PVA) as a stabilizer and $FeCl_3$ as an initiator.[55] The mixture of pyrrole (Py) and and pyrrole-1-propanoic acid (COOH-Py) with different molar ratios was introduced into the aqueous dispersion of PVA and $FeCl_3$, resulting in the formation of the PPy NPs with –COOH groups on the particle surface. It was found that the UV–vis absorbance of the obtained COOH-PPy NPs at 808 nm decreased as the molar ratio of Py to COOH-Py decreased (Figure S1, Supporting Information). PPy NPs without COOH-Py owed the highest absorbance while COOH-PPy NPs with 90% COOH-Py had the lowest absorbance. Based on the consideration of theranostic modification, the optimal molar ratio of Py to COOH-Py should be 7:3 since the nanoparticles with this molar ratio showed a relatively high UV–vis absorbance and a relatively large amount of carboxyl groups on the particle surface for further conjugation of functional molecules, such as PEG and Gd-DOTA.

NH_2-PEG-NH_2 was then conjugated to the surface of COOH-PPy NPs through the formation of stable amide bonds with NHS and EDC as coupling agents, obtaining NH_2-PEG-PPy NPs with free amine groups on the surface. The successful conjugation of NH_2-PEG-NH_2 to the surface of COOH-PPy NPs was characterized by FT-IR spectra (Figure S2, Supporting Information). COOH-PPy NPs showed shoulder peaks at 1729 cm^{-1} for the stretching vibration band due to the C=O in the free carboxyl group. After the conjugation, this characteristic band disappeared while leaving only a characteristic band assigned to the -CONH- group at around 1645 cm^{-1}, indicating the reaction of NH_2-PEG-NH_2 with the free carboxyl groups on the surface of COOH-PPy NPs. ^1H NMR spectra were further used to characterize the grafting of PEG onto the PPy particles surface (Figure S3, Supporting Information). The COOH-PPy NPs showed merely a water peak (δ 4.7 ppm). On the contrary, an additional peak of PEG chain could be clearly detected as a symmetric singlet (δ 3.6 ppm) for the NH_2-PEG-PPy NPs. It

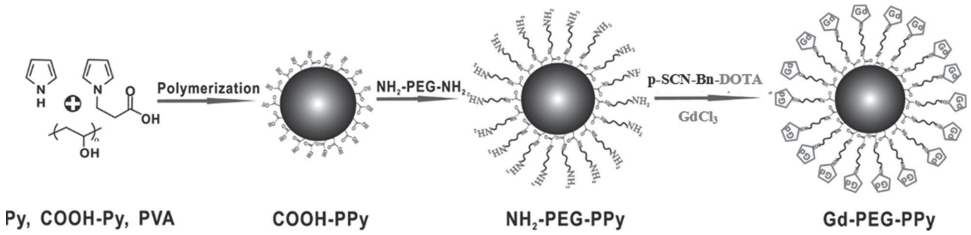

Scheme 1. Schematic illustration of the fabrication process of Gd-PEG-PPy NPs.

provided a strong evidence that NH_2-PEG-NH_2 was successfully conjugated onto the surface of PPy NPs. Then, Gd^{3+} chelator of p-SCN-Bn-DOTA with active -SCN group was added and induced amide formation between NH_2-PEG-PPy NPs and DOTA in the phosphate buffer solution (PBS) buffer. The zeta potential of the nanoparticles changed from –27.21 ± 1.99 mV to –9.15 ± 0.86 mV after the PEG-bis-amine conjugation, and then back to –38.68 ± 2.61 mV after p-SCN-Bn-DOTA conjugation (Figure S4, Supporting Information).

Finally, Gd^{3+} was chelated into the DOTA ligand by heating $GdCl_3$ with the resulting DOTA-PEG-PPy NPs at pH 5.8. After chelation, the zeta potential of Gd-PEG-PPy NPs showed an obvious increase to –15.43 ± 0.73 mV due to the coordination of cationic Gd^{3+} ions with the carboxylate groups of the DOTA ligand (Figure S4, Supporting Information). Although the zeta potential is somewhat low, the negative charge is sufficiently strong to ensure a good colloidal stability with the assistance of the neutral PVA surfactant and PEG molecules on the surface of the particles. The TEM images revealed that the Gd-PEG-PPy NPs had a uniform diameter of about 69.3 ± 2.1 nm (**Figure 1**b), slightly higher than that of COOH-PPy NPs (64.9 ± 1.9 nm) (Figure 1a). This result was well consistent with the hydrodynamic diameters which were evaluated by the DLS measurements (Figure S5, Supporting Information). The bigger particle size of Gd-PEG-PPy NPs should be mainly due to the introduction of PEG coatings on the nanoparticle surface. Moreover, the concentration of gadolinium as well as the number of Gd^{3+} ions per Gd-PEG-PPy NP was determined using inductively coupled plasma optical emission spectrometry (ICP-OES). Determination of the Gd-PEG-PPy NPs concentration followed by theoretical calculation based on the average size of 70 nm revealed the total number of Gd^{3+} ions per Gd-PEG-PPy NP to be about 2.93×10^3.[11] All these results convinced that the Gd chelates were successfully attached to the surface of Gd-PEG-PPy NPs, which provided the basis for further MRI experiments.

The stability of the Gd-PEG-PPy NPs were investigated by incubating these nanoparticles in various biological mediums, including PBS, RPMI-1640 cell medium, fetal bovine serum (FBS), and simulated body fluid (SBF). As shown in Figure S6A, S6B in the Supporting Information, the Gd-PEG-PPy NPs were well dispersed and exhibited excellent stability in all these biological mediums. No precipitation was observed and no obvious change in hydrodynamic particle size was found in the PBS solutions after 1 week storage (Figure S6C, Supporting Information), allowing these nanoparticles to be further used in biological systems. Gd-PEG-PPy NPs maintained strong absorption in the NIR region as compared to the initial COOH-PPy NPs (Figure 1c). An important feature of Gd-PEG-PPy NPs is their NIR light-induced thermal effect, which could be used for photothermal therapy. Figure 1d shows the temperature change of an RPMI-1640 culture medium containing Gd-PEG-PPy NPs with different concentrations. Under NIR laser irradiation (808 nm, 1.5 W cm^{-2}, 10 min), the control RPMI-1640 sample without Gd-PEG-PPy NPs showed little temperature change. In contrast, the temperature of the

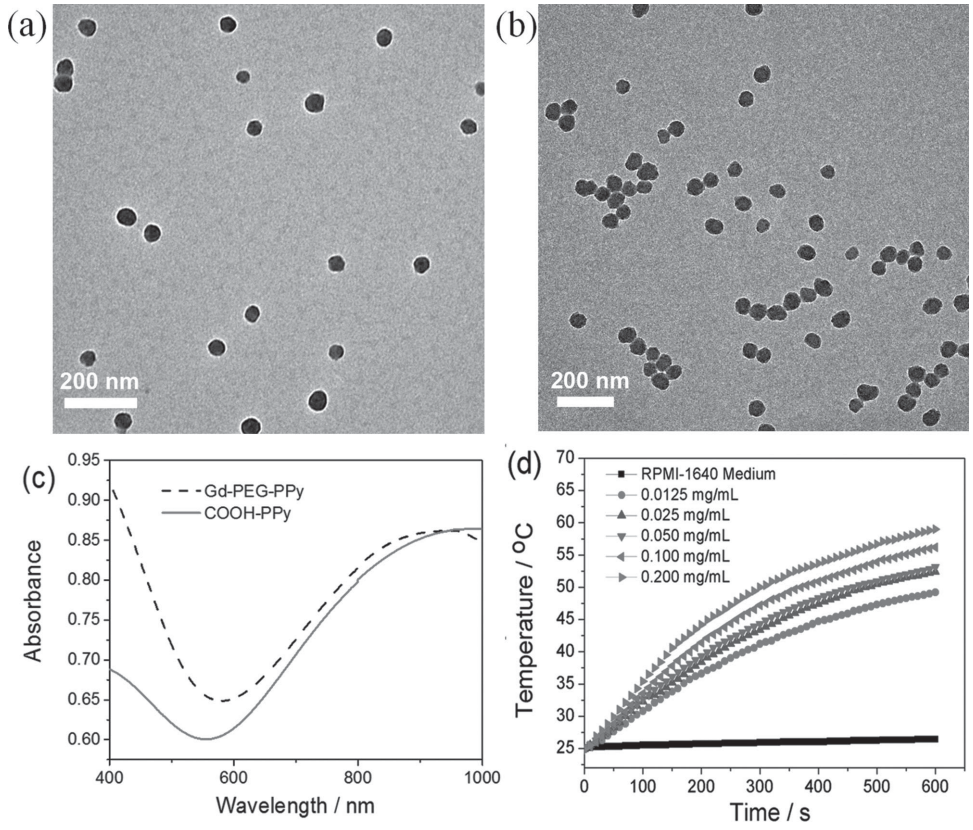

Figure 1. TEM images of a) COOH-PPy NPs and b) Gd-PEG-PPy NPs. c) UV–vis–NIR absorption spectra of COOH-PPy NPs and Gd-PEG-PPy NPs solutions at the same concentration. d) Heating curves of RPMI-1640 medium containing different concentrations of Gd-PEG-PPy NPs under an 808-nm laser irradiation at a power density of 1.5 W cm^{-2} for 10 min.

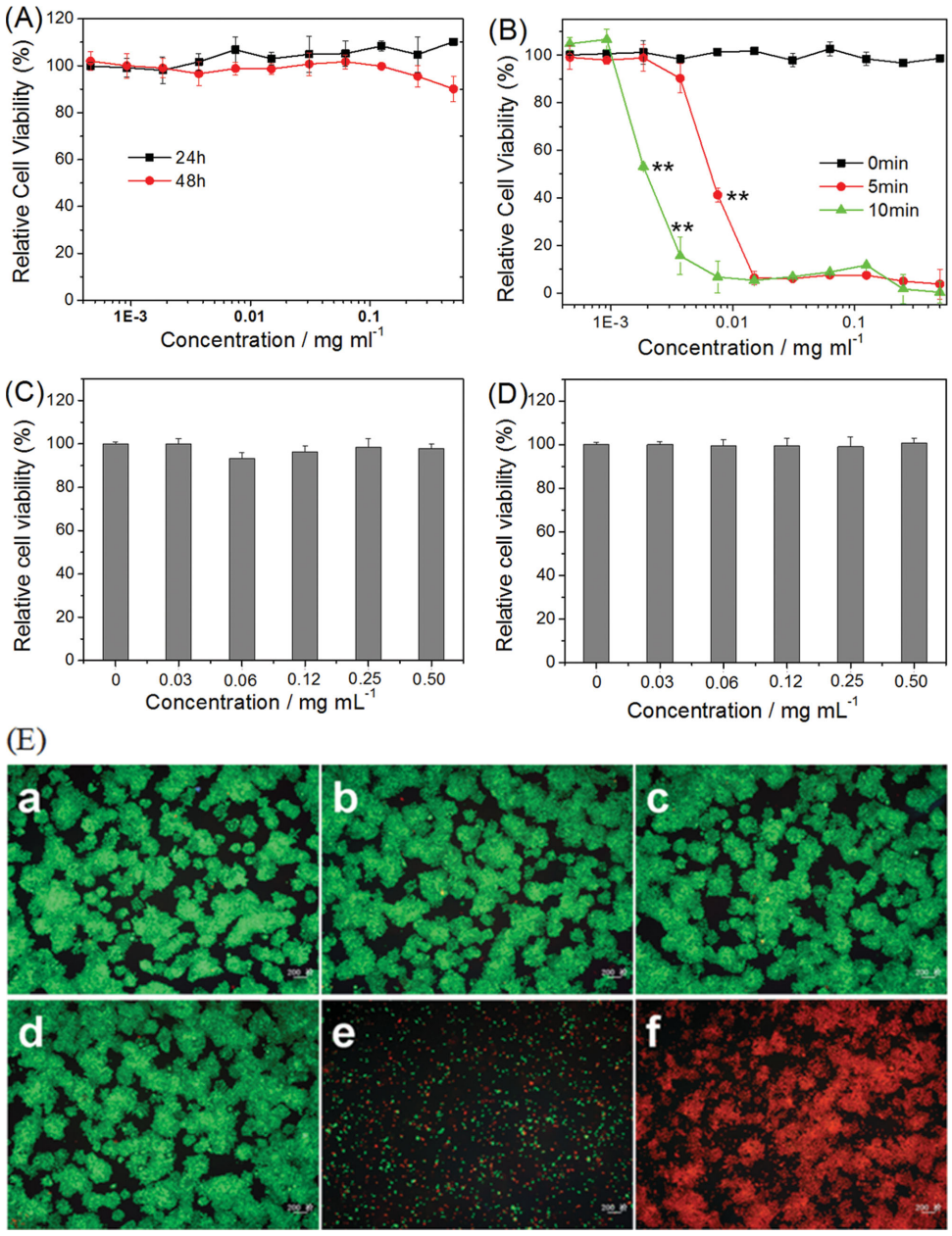

Figure 2. A) Relative cell viability of HUVECs after treatment with different concentrations of Gd-PEG-PPy NPs for 24 h and 48 h. B) Relative cell viability of HeLa cells treated with different concentrations of Gd-PEG-PPy NPs and NIR laser irradiation for different time, $^{**}p < 0.01$ versus control without light irradiation. Cytotoxicity of Gd-PEG-PPy NPs to BMDC cells C) and T cells D) as determined by MTT assay. E) Photothermal killing effect of Gd-PEG-PPy NPs to HeLa cells: a) no Gd-PEG-PPy NPs and no laser irradiation; b,c) laser irradiation only for 5 min and 10 min, respectively; d) 0.005 mg mL^{-1} Gd-PEG-PPy NPs only; e,f) 0.005 mg mL^{-1} Gd-PEG-PPy NPs combined laser irradiation for 5 min and 10 min, respectively. (NIR laser: 808 nm, 1.5 W cm^{-2}).

Gd-PEG-PPy NPs solution (25 μg mL^{-1}) increased from 25 to 52 °C, which is sufficient to kill tumor cells.[56]

2.2. In Vitro Cytotoxicity and Photothermal Effect of Gd-PEG-PPy NPs

Excellent biocompatibility was very important for the application of a new theranostic agent. In vitro cytotoxicity of Gd-PEG-PPy NPs was first studied by 3-(4,5)-dimethylthiahiazo(-z-y1)-3,5-di-pheny-tetrazolium-romide (MTT) assay for testing the standard cell viability of four kinds of cells, including normal cell line of human umbilical vein endothelial cells (HUVEC), tumor model of human cervical carcinoma cells (HeLa cells), immunity cells of bone marrow dendritic cells (BMDCs), and T cells. It was found that HUVECs and HeLa cells exhibited the cell viability higher than 90% even at a high Gd-PEG-PPy NPs concentration of 0.5 mg mL^{-1} after 24 or 48 h of incubation (**Figure 2**A and 2B).

Similarly, Gd-PEG-PPy NPs exhibited little cytotoxicity to both BMDC and T cells from SD rats (Figure 2C,D). Cells survival was then detected by staining with both calcein acetoxymethyl ester (calcein AM) and propidium iodide (PI) (Figure S7, Supporting Information). Fluorescence microscopy images showed that the BMDC cells and T cells treated with 0.5 mg mL^{-1} Gd-PEG-PPy NPs for 24 h exhibited bright green color and no dead cells were observed, well consistent with the MTT results. For further investigating the in vivo toxicity in mice, a high dose of Gd-PEG-PPy NPs (200 µL, 10 mg mL^{-1} per mouse) was intravenously administered. Histological sections of vital organs (heart, liver, spleen, lung, and kidneys) stained with hematoxylin and eosin did not show any apparent injury in cellular structures at 1 day, 7 days and 25 days after intravenous administration of Gd-PPy-PEG NPs (Figure S8, Supporting Information). All these data indicated that the Gd-PEG-PPy NPs had good biocompatibility. Although gadolinium complexes used for MRI are reported to cause cardio toxicity,[57,58] macrocyclic Gd-DOTA showed greater stability than the conventional linear Gd-DTPA complexes, which theoretically might reduce biological interactions in man. Gd-DOTA has been reported to show no direct deleterious effect on cardiac electrophysiology and especially on ventricular repolarization.[57,58] Thus, the use of Gd-DOTA as an MRI-enhancing contrast medium in the clinical practice setting appears to be safe and effective.

Photothermal effect of Gd-PEG-PPy NPs were further demonstrated at the cellular level. We chose HeLa cells as model cells to test the nanoparticle concentration-dependent photothermal cancer cell killing using a standard MTT assay (Figure 2B). As expected, HeLa cells treated with Gd-PEG-PPy NPs without laser irradiation exhibited little toxicity. In contrast, the cell viability significantly decreased when they were treated with Gd-PEG-PPy NPs followed by laser irradiation (808 nm and 1.5 W cm^{-2}) for 5 and 10 min, respectively. The photothermal killing efficiency increased with increasing the concentration of Gd-PEG-PPy NPs and laser irradiation time. After 5 min of laser treatment, only less than 40% of HeLa cells remained viable at the Gd-PEG-PPy NPs concentration of 0.01 mg mL^{-1}. These results were also proved by the calcein-AM/PI stained cell images (Figure 2E). Cells treated with only laser irradiation or Gd-PEG-PPy NPs alone showed green fluorescence of calcein, which indicated the survival of HeLa cells, suggesting that exposure of cancer cells to either Gd-PEG-PPy NPs or a NIR laser alone caused almost no cell death (Figure 2E(a-d)). On the contrary, the treatment with Gd-PEG-PPy NPs in combination with NIR laser irradiation induced obvious cell killing (Figure 2E(e) and 2E(f)). In addition, longer laser irradiation time led to more effective cell death (Figure 2E(f)). These results clearly revealed that the Gd-PEG-PPy NPs could be an effective PTT agent.

2.3. In Vitro and In Vivo MRI

The MR imaging capability of Gd-PEG-PPy NPs were then investigated by measuring T_1 as a function of aqueous nanoparticles with different concentrations, which were determined using ICP-OES. **Figure 3**A showed T_1-weighted MR images with the incremental signal intensity indicated by the enhanced brightness in the range of Gd^{3+} ion concentrations from 18.75 to 300×10^{-6} M. T_1 relaxation time increases with the concentrations of Gd^{3+} ion increasing and the trend is well fit by a linear line within the analyzed range of Gd^{3+} ion concentrations, revealing the concentration-dependent lighting effect. A high T_1 relaxivity coefficient (r_1) value of 10.61 L mM^{-1} s^{-1} was acquired on a 3T MR scanner for Gd-PEG-PPy NPs (Figure 3B). This value was more than two times as high as that of Gd^{3+} DOTA (r_1 = 4.2 L mM^{-1} s^{-1}) under a 3 T magnetic field. It has been reported that the r_1 values of various paramagnetic metal complexes could be highly enhanced by conjugating them onto the nanoparticle surface due to the reduction of tumbling rate of those paramagnetic metal complexes and the effective interaction between water and the paramagnetic metal complexes.[59,60] Hence, the r_1 relaxivity of Gd-PEG-PPy NPs was strongly enhanced due to grafting Gd^{3+} DOTA onto the PPy NPs surface and the introduction PEG spacers. The results imply that the present Gd-PEG-PPy NPs would be a promising candidate as a contrast agent for MR imaging of cancers.

To examine whether Gd-PEG-PPy NPs can be used to identify the tumors in living mice, MR images of mice bearing U87-MG tumor were acquired at different time periods (preinjection, 1, 18, and 24 h) after intravenous tail injection of Gd-PEG-PPy NPs (100 µL, 5 mg mL^{-1}). Figure 3C,D showed the MRI signal and intensity distributions as a function of time for Gd-PEG-PPy NPs delivered systemically via tail vein injections. In the preinjection image, there were little intrinsic contrast between the tumors and surrounding tissue. At 1 h after Gd-PEG-PPy NPs injection, a slight MRI signal enhancement could be observed, and MR signals at the tumor sites gradually became stronger over time. After 24 h postinjection, the MRI signals reached a maximum and almost located inside the tumor. This suggested that large amount of Gd-PEG-PPy NPs circulated in the blood circulation and then accumulated at the tumor site, which proved the high efficiency of tumor targeting of these nanoparticles. Because of the enhanced permeation and retention (EPR) effect of cancerous tumors, Gd-PEG-PPy NPs around 69 nm could be passively accumulated into tumor.[61] In addition, the introduction of the PEG layer onto the surface of PPy NPs contributes to the inhibition from the macrophage recognition at reticuloendothelial system (RES) of liver and spleen due to the excellent hydration property of PEG layer, resulting in a prolonged circulation time in blood. The tumor sites exhibited obvious enhancement in T_1-weighted MRI intensity compared with that before injection, indicating that Gd-PEG-PPy NPs remain in the tumor sites more than 24 h to provide adequate time for the following photothermal therapy. The passive targeting and high MRI contrast ability of Gd-PEG-PPy NPs are favorable for precise cancer diagnosing and locating the tumor site to guide the external NIR laser irradiation for photothermal ablation of tumors in avoidance of damaging the surrounding healthy tissues.

2.4. In Vivo Photoacoustic Imaging

The possibility of Gd-PEG-PPy NPs with strong NIR absorption to serve as a photoacoustic imaging contrast agent was evaluated

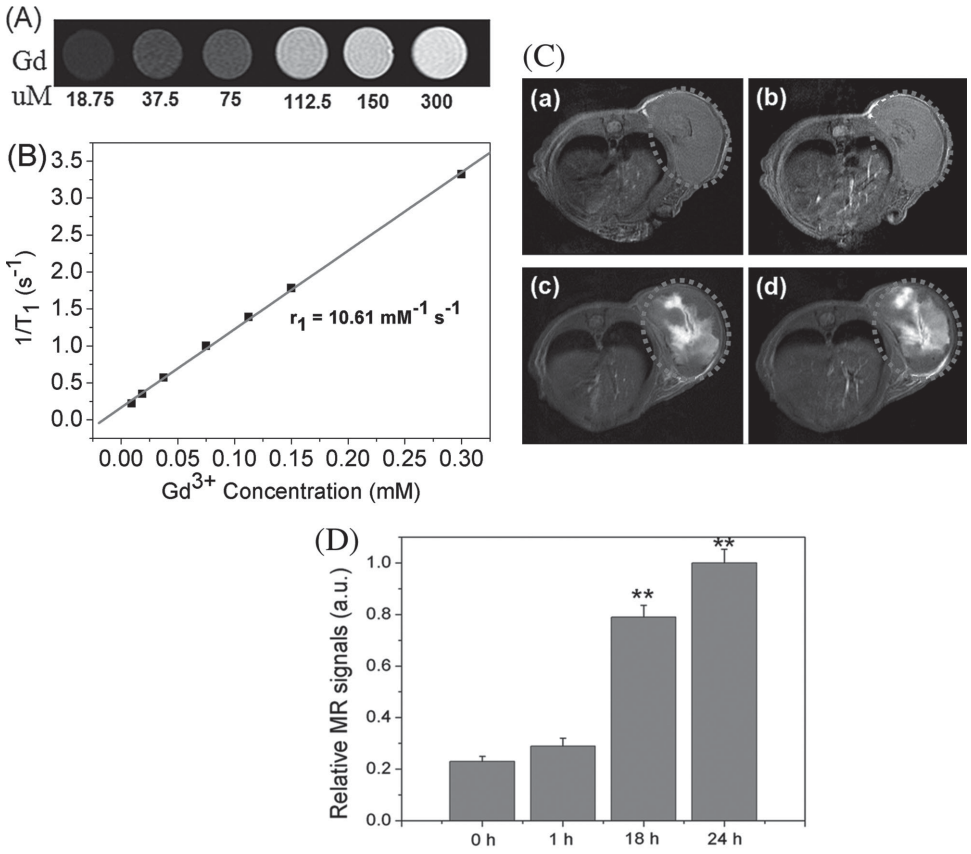

Figure 3. A) In vitro phantom MRI contrast images of Gd-PEG-PPy NPs at different concentrations:18.75, 37.5, 75, 112.5, 150, 300 × 10^{-6} M; B) Linear fitting of the $1/T_1$ value as a function of Gd^{3+} concentration in 0.9% saline; C) In vivo T_1-weighted MRI imaging of mice a) before, b) 1 h, c) 18 h, and d) 24 h after intravenous injection of Gd-PEG-PPy NPs. The circles indicate the tumor; D) The normalized signal intensity of T_1-weighted MR signals from the tumor at different time post injection, $^{**}p < 0.01$ versus 0 h or 1 h after injection.

on a U87-MG tumor bearing mouse (**Figure 4**a), which was imaged before and after a single injection of Gd-PEG-PPy NPs (100 μL, 5 mg mL^{-1}). Compared with intrinsic tumor image with only big vasculatures visible (Figure 4c) before injection, the PA image showed greater clarity and significant increase in the PA signal in the tumor after 24 h intravenous injection of Gd-PEG-PPy NPs (Figure 4d,e). The significantly increased photoacoustic signals in the tumor was attributed to the strong absorption of NIR laser pulses by Gd-PEG-PPy NPs, providing an additional evidence for the high tumor accumulation of Gd-PEG-PPy NPs after a long-time circulation in blood vessels. Together with MRI imaging, the combination of the two types of in vivo imaging contrasting abilities enable Gd-PEG-PPy NPs to acquire the detailed structure of tumor region, showing great prospect for imaging guided photothermal therapy.

Gd-PEG-PPy NPs were passively delivered to the tumors tissues through the EPR effect with high efficiency, which made them enter the extravascular space from the systemic circulation, facilitating to accumulate around tumor cells.[62,63] However, heterogeneity in tumor blood supply and interstitial flow and physiological barriers may induce heterogeneous localization of nanoparticles within the tumor.[64] In addition, the EPR effect is very heterogeneous in nature and varies between different tumor types since different tumors have different pore dimensions in the vasculature. Thus, Gd-PEG-PPy NPs may not work for all kinds of tumors. Future work should be focusing on actively targeting to tumors by surface modifications of these nanoparticles with specific targeting moieties.[65,66]

2.5. In Vivo Blood Circulation and Biodistribution

To confirm the imaging results, the in vivo blood circulation and biodistribution of Gd-PEG-PPy NPs were examined after intravenous injection by measuring the Gd^{3+} levels in blood samples and various organs using inductively coupled plasma mass spectrometry (ICP-MS). As shown in **Figure 5**a, Gd-PEG-PPy NPs displayed a prolonged blood circulation time. The half-life of Gd-PEG-PPy NPs was determined to be 12.47 ± 1.97 h, much longer than non-PEGylated PPy NPs (12 min).[49] Biodistribution data of Gd-PEG-PPy NPs based on Gd^{3+} levels at 24 h postinjection showed that Gd-PEG-PPy NPs were relatively low in heart, kidney, and lung. In contrast, high levels of Gd element were observed in the tumor, as well as reticuloendothelial systems (RES) such as liver and spleen (Figure 5b). The tumor uptake was measured to be about 18.0% ID g^{-1} at 24 h post injection. This is likely due to the PEG coating on the surface of Gd-PPy-PEG NPs, which can delay their macrophage clearance during blood circulation and favor to accumulate in the tumor by the EPR effect, especially those with long blood circulation time.

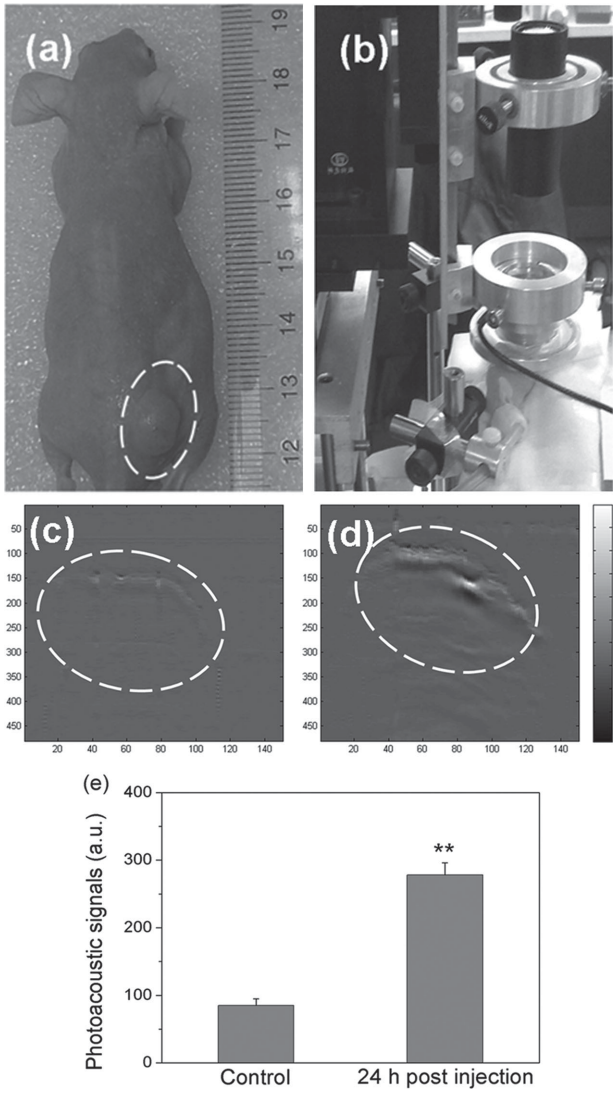

Figure 4. In vivo photoacoustic imaging. a) Photograph of the nude mice tumor before the data acquisition. b) Photograph of experimental setup. Photoacoustic images of mice before c) and d) 24 h after the tail intravenous injection of Gd-PPy-PEG NPs (100 μL, 5 mg mL^{-1}). White circles highlight the tumor site. e) The quantification of photoacoustic signals from the tumor site in (c) and (d), $^{**}p < 0.01$ versus control.

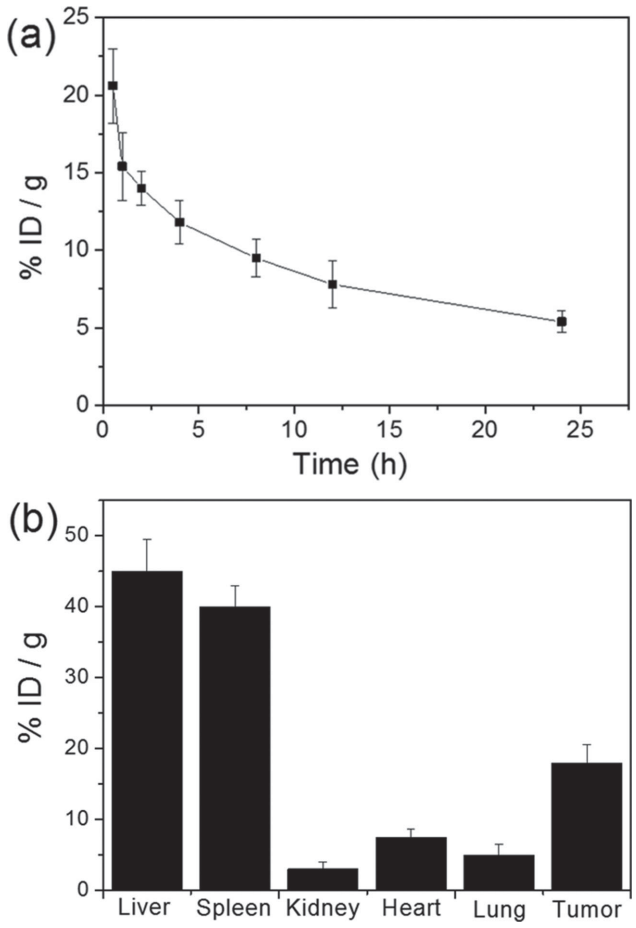

Figure 5. a) Blood circulation and b) Biodistribution of Gd-PEG-PPy NPs after intravenous injection into healthy or tumor bearing mice as determined by measuring Gd^{3+} concentrations in tissue lysates using ICP-MS. Error bars were based on the standard error of the mean (SEM) of triplicate samples. The unit was the percentage of injected dose per gram tissue (%ID g^{-1}).

2.6. In Vivo Photothermal Therapy

The strong in vitro photothermal effect of Gd-PEG-PPy NPs shown in the cell experiments together with the high tumor accumulation of these nanoparticles as uncovered in MR/photoacoustic imaging experiments inspired us to use them for in vivo cancer PTT treatment. Female BALB/c mice bearing U87-MG tumor were divided into 6 groups with 8 mice in each group: agent (i.v.) only, agent (i.t.) only, saline (i.t.) only, agent (i.v.) + laser, agent (i.t.) + laser, saline (i.t.) + laser. (Here, i.v. denotes intravenous injection, and i.t. denotes intratumoral injection.) Gd-PEG-PPy NPs suspension in saline were intravenously (100 μL, 5 mg mL^{-1}) and intratumorally (100 μL, 2 mg mL^{-1}) injected into the mice of agent (i.v.) only, agent (i.t.) only, agent (i.v.) + laser and agent (i.t.) + laser groups, respectively. After 24 h injection, the tumor areas of the mice in the three laser groups with continuous anesthesia were exposed to the 808 nm laser irradiation at the power density of 1.5 W cm^{-2} for 10 min. The tumor temperature change was monitored during laser irradiation (**Figure 6**A). In the agent (i.v.) + laser group the temperature in the tumor areas rapidly increased to about 53 °C within 2 min, and maintained at this temperature for nearly 8 min, which was enough to destroy the tumor in vivo. Similar result was observed for the local intratumorally injected agent (i.t.) + laser group, showing slightly higher temperature of about 55 °C because of relatively higher concentration of Gd-PEG-PPy NPs in tumor area by intratumoral injection. In marked contrast, the control group without Gd-PEG-PPy NPs injection only showed slight increase to about 40 ºC within 10 min of laser irradiation, indicating that NIR laser irradiation at this condition could not cause damage to the tumors.

The therapeutic effectiveness was evaluated by measuring the tumor sizes of each group at certain day after treatment (Figure 6B). It was found that inoculated tumors grew rapidly over time in the groups of agent (i.v.) only, agent (i.t.) only, saline

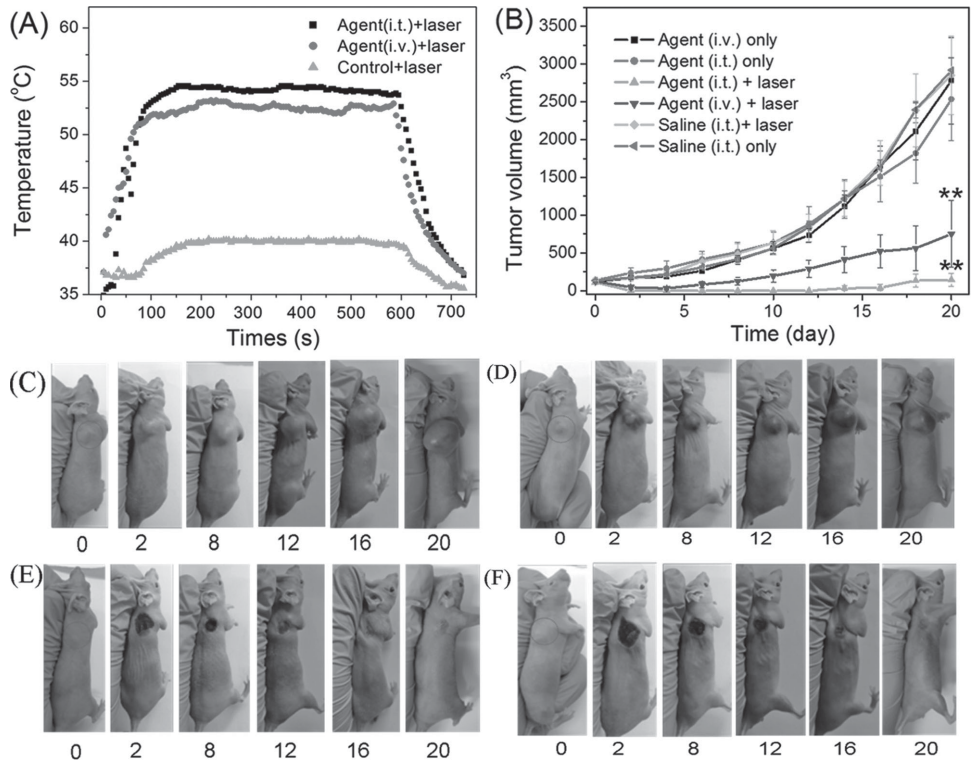

Figure 6. A) Temperature change curves of the nude mice tumor after treatments with saline or Gd-PEG-PPy NPs (tail vein or tumor injection) in combination with exposure to the 808 nm laser at a power density of 1.5 W cm^{-2}; B) Quantitative measurement of tumor volume in mice after different treatments, $^{**}p < 0.01$ versus saline or laser or agent only treatment. Representative photographs of tumors in mice before and after various treatments for 2 d, 8 d, 12 d, 16 d, and 20 d; C) tail vein injection of Gd-PEG-PPy NPs only; D) tumor injection of Gd-PEG-PPy NPs only; E) tail vein injection of Gd-PEG-PPy NPs and NIR laser irradiation; F) tumor injection of Gd-PEG-PPy NPs and NIR laser irradiation. (Circles indicate the tumor)

(i.t.) only and saline (i.t.) + laser, showing similar tumor growth rate. For the agent (i.v.) only groups, tumor volume increased from 136.6 mm^3 to approximately 2783 mm^3 at 20 days after treatment. These results indicated that either Gd-PEG-PPy NPs or NIR laser irradiation alone did not affect the tumor growth. In stark contrast, the tumors were effectively inhibited in both agent (i.v.) + laser and agent (i.t.) + laser groups. At 20-day after treatment, the tumor volume was maintained at about 150.5 mm^3 for the intratumoral injection group while from 135.0 mm^3 to 761.6 mm^3 for the intravenously injection group. It was well in agreement with the tumor temperature measurements, where higher temperature was obtained for the agent (i.t.) + laser group. The above results revealed that Gd-PEG-PPy NPs in combination with NIR laser exposure could ablate tumor tissue efficiently, which was further confirmed by the representative mice photographs recorded before and after different treatments. Compared to the control groups (Figure 6C,D), excellent therapeutic effectiveness of the agent + laser groups could be clearly observed, leaving black scars at the original tumor sites (on the diseased tissue) that fell off after about 16 days (Figure 6E,F). Therefore, Gd-PEG-PPy NPs could be used as a powerful photothermal agent for in vivo PTT treatment of cancer.

The potential in vivo toxicity of Gd-PEG-PPy NPs was also investigated. Change of mice body weight was usually used as a method for testing the treatment induced toxicity. As shown in **Figure 7**a, no apparent difference was observed among different groups within 20 days of observation, suggesting that all treatments were tolerated well by the tumor-bearing mice and the photothermal treatment showed no obvious sign of toxic effect. 20 days after treatment, the vital organs of mice including heart, liver, spleen, lung, kidney, and tumor were collected and used for further histological examination. Hematoxylin and eosin (H&E) stained images showed that the tumor tissues were disappeared after Gd-PEG-PPy NPs injection followed by laser irradiation. In contrast, neither noticeable organ damage nor inflammation could be observed in all major organs of the treated mice (Figure 7b), indicating that Gd-PEG-PPy NPs induced no obvious side effect to the treated animals. It only exerted cytotoxicity after NIR laser irradiation, showing an enormous advantage over traditional chemotherapeutic drugs.

Many other hyperthermic methods, such as radiofrequency (RF), microwaves, magnetic fields, or ultrasound, have been used to heat tumors to cause irreversible cellular damage and ultimately result in cell death. However, there are still some limitations due to their damage to surrounding healthy tissue.[67] In contrast, Gd-PEG-PPy NPs mediated photothermal therapy can confine thermal damage to the tumor by carefully control the light irradiation and selectively heat the target area under the guidance of MRI/PAI bimodal imaging.

Compared with other conjugated polymers based theranostic agents, Gd-PEG-PPy NPs show a prolonged blood circulation time and an effective tumor accumulation. In addition,

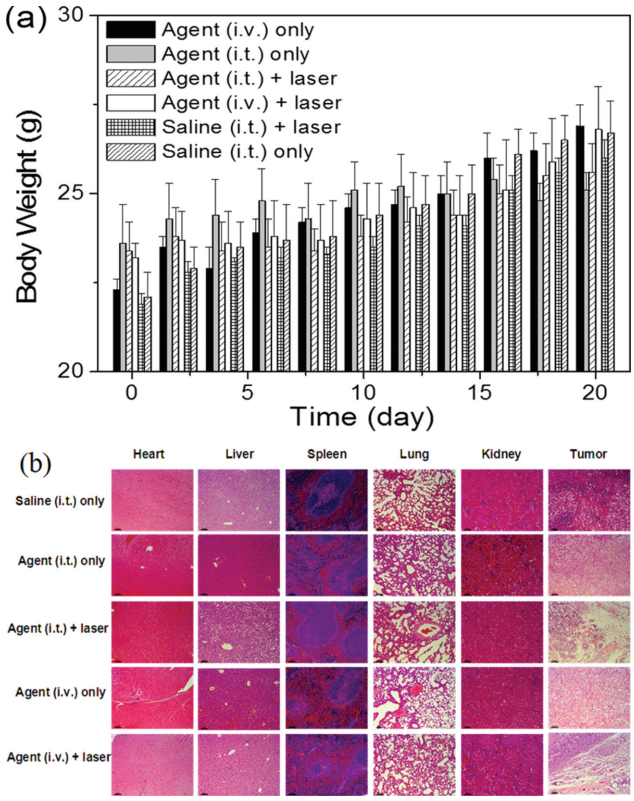

Figure 7. a) Body weights of mice at different time points after various treatments; b) Histology staining of tissues slices (heart, liver, spleen, lung, kidney, and tumor) collected from different groups of mice 20 days after treatment.

polypyrrole is a material showing superior biocompatibility,[52,53] and Gd-DOTA is also a safe and effective MRI-enhancing contrast agent.[57,58] Therefore, Gd-PEG-PPy NPs, the conjugate of polypyrrole and Gd-DOTA, would be a very promising nanotheranostic agent for accurately visualizing the size and location of the tumor, guiding and monitoring the therapeutic process.

A major drawback of Gd-PEG-PPy NPs is its lack of specific or active targeting of tumor tissues. Further modifying this materials with tumor-homing ligands for its specific cancer theranostics is needed to extend its applications. On the other hand, the long-term in vivo toxicity of Gd-PEG-PPy NPs is a primary concern. PPy has been widely used in biosensors, drug delivery and nerve regeneration, its biocompatibility has been extensively studied in vitro and in vivo and shows no reports of major toxicity issues.[68–70] Nevertheless, its elimination from the body is still unclear and needs further systematic investigation.

3. Conclusion

In summary, we have successfully constructed a theranostic agent of Gd-PEG-PPy NPs with excellent physiological stability, strong NIR absorption, and high magnetization. Gd-PEG-PPy NPs showed little appreciable dark toxicity and highly effective cancer cell ablation upon irradiation of NIR light in vitro. Based on the bi-modal MR/PAT imaging ability of Gd-PEG-PPy NPs, tumor site and size of the treated mice could be clearly identified, indicating passive targeting and efficient accumulation of Gd-PEG-PPy NPs. Significant tumor ablation was achieved after both systemic and tumor local administration of Gd-PEG-PPy NPs, followed by NIR laser irradiation. In addition, histological examination demonstrated no apparent toxicity of Gd-PEG-PPy NPs to the treated mice during the whole study period. Therefore, Gd-PEG-PPy NPs hold great potential for accurate cancer diagnosing and locating the tumor site to guide the external NIR laser irradiation for efficient photothermal ablation of tumors without damaging the surrounding healthy tissues.

4. Experimental Section

Materials: Pyrrole, pyrrole-1-propanoic acid, and polyvinyl alcohol (PVA, 86–89% hydrolyzed, 10 kDa MW), PEG-bis-amine (98%, 3350 MW), *N*-hydroxysuccinimide (NHS) and 1-ethyl-3-(3-dimethylaminopropyl) carbodiimide (EDC) were purchased from Sigma–Aldrich. p-SCN-Bn-DOTA (1,4,7,10-Tetraazacyclododecane-1,4,7,10-tetraacetic acid, 2-[(4-isothiocyanatophenyl)methyl]-) was obtained from Macrocyclics. Propidium iodide (PI) and calcein acetoxymethyl ester (calcein AM) were the products of Sigma–Aldrich. 3-(4,5)-dimethylthiahiazo(-z-y1)-3,5-di-pheny-tetrazolium-romide (MTT) was purchased from Beijing Biotopped Science&Technology Co., Ltd. Deionized (DI) water (18.2 MΩ cm) was obtained by a Milli-Q Water Purification system. Simulated body fluid (SBF) were prepared according to the literature.[71] All other chemicals and reagents were of analytical grade and used without further purification.

Synthesis of Gd-PEG-PPy Nanoparticles: COOH-PPy NPs were synthesized through the microemulsion method.[47,52] Briefly, 1.0 g PVA (≈10 kDa) was first dissolved in 40 mL deionized water by magnetically stirring at 60 °C for 20 min. After cooling to room temperature, $FeCl_3{\cdot}6H_2O$ (1.26 g) was added, followed by stirring for 30 min. After cooling to 5 °C, the mixture of Py and COOH-Py (2 mol) with different molar ratio of 10:0; 9:1; 7:3; 5:5; 3:7; 1:9 was added dropwise to the reaction solution. The polymerization proceeded while stirring and the mixture solution turned black within a few minutes. After polymerization for 24 h, the resulting black dispersion was washed for several times by using ultrafiltration filters with molecular weight cut off (MWCO) of 100 kDa which could remove excess PVA. The COOH-PPy NPs were then modified with PEG-bis-amine according to the reported method.[72] Briefly, 1 mL of COOH-PPy NPs aqueous dispersion (5 mg mL^{-1}) was incubated with 50 µL l50 mg mL^{-1} EDC and 50 µL 150 mg mL^{-1} NHS for 20 min at room temperature with gentle stirring. The resulting NHS-activated NPs were then covalently linked to PEG-bis-amine (90 mg mL^{-1}). The resulting NH_2-PEG-PPy NPs were purified by ultrafiltration filters with MWCO of 100 kDa and dispersed in PBS buffer for subsequent experiments. NH_2-PEG-PPy NPs were conjugated with chelator of p-SCN-Bn-DOTA according to the literature.[73] In brief, NH_2-PEG-PPy was dispersed in PBS buffer (0.1M, pH8.5) at a concentration of 20 mg mL^{-1} and mixed with 20-molar excess of p-SCN-Bn-DOTA (50 mg mL^{-1}) dissolved in ethanol. The reaction mixture was slowly stirred at 4 °C for 24 h. Excess chelator was removed from the solution of DOTA-PEG-PPy NPs by ultrafiltration filters with MWCO of 100 kDa. The $GdCl_3$ was mixed with the DOTA-PEG-PPy NPs suspension with a 20:1 molar ratio of Gd(III) to DOTA-PEG-PPy.[74] The mixture was sealed in a 10 mL vial under continuous stirring in an oil bath at 70 °C for 2 h. After cooling down to room temperature, Gd-PEG-PPy NPs were purified by several cycles of washing/centrifuging to remove excess Gd(III) ions using acetate buffer (pH 5.8) and PBS (10×10^{-3} M, pH 7.4), respectively.

Nanoparticle Characterization: UV–vis absorption spectra of the nanoparticles at different fabrication stages were analyzed using a UV–vis spectrophotometer (Varian Cary 4000) with a quartz

cuvette of 1 cm optical path length. Fourier-transform infrared (FT-IR) spectra of the nanoparticles were recorded using a FT-IR spectrometer (Varian 3100) in the transmission mode using KBr powder as pellet press materials. The size distributions and zeta potentials of the nanoparticles were evaluated by a 90Plus/BI-MAS instrument (Brookhaven Instruments Co., U.S.A). The morphology of the nanoparticles was observed using a FEI Tecnai G2 Sphera transmission electron microscope (TEM) with the accelerating voltage of 120 kV. Determination of Gd contents of Gd-PEG-PPy NPs in vitro and in vivo was performed by inductively coupled plasma optical emission spectrometry (ICP-OES) and inductively coupled plasma mass spectrometry (ICP-MS) after decomposing the Gd-PEG-PPy NPs containing samples by aqua regia. A noncompartmental pharmacokinetic analysis using the KineticaTM software package (version 5.0, Thermo Fisher Scientific Inc., MA, USA) was performed to determine the key parameter of half-life ($t_{1/2}$). Photographs of the aqueous dispersions of the nanoparticles were taken by a digital camera (Canon 600D).

Measurement of Photothermal Effect of Gd-PEG-PPy NPs: Different concentrations of Gd-PEG-PPy NPs solutions dispersed in RPMI-1640 medium (total volume of 3.0 mL) were placed in a quartz cuvette, then irradiated using a continuous-wave diode 808 nm NIR laser (Xi'an Minghui Optoelectronic Technology, China) with an output power density of 1.5 W cm^{-2} for 10 min. The temperature was monitored and periodically measured by a digital thermometer with a thermocouple probe at 10 s interval. RPMI-1640 medium without nanoparticles were also exposed to the NIR laser light as controls. The heating curve was determined by plotting the measured temperature to the irradiation time.

Cell Culture: The human cervical carcinoma cells (HeLa) originally obtained from American Type Culture Collection (ATCC) were cultured in RPMI-1640 medium (GIBCO) with 10% fetal bovine serum (FBS) at 37 °C in a humidified atmosphere containing 5% CO_2. Bone marrow dendritic cells (BMDC) were generated by culturing bone marrow stem cells from SD rats in complete IMDM (Iscove's Modified Dulbecco's Medium) with 20 ng mL^{-1} recombinant granulocyte/macrophage colony stimulating for 6 days at 37 °C and T cells obtained from SD rats were cultured in cIMDM at 37 °C.

In Vitro and In Vivo Biocompatibility of Gd-PEG-PPy NPs: Biocompatibility of the Gd-PEG-PPy NPs to four kinds of cells, including HeLa cells, HUVECs (Human Umbilical Vein Endothelial Cells), BMDC cells, and T cells, were investigated by the MTT assay. Briefly, HeLa cells and HUVECs cells were first seeded in 96 well plates (1×10^5 cells per well) in a humidified atmosphere containing 5% CO_2 for 24 h. The cell culture medium was then replaced with 0.2 mL fresh culture medium containing different concentrations of the nanoparticles from 0 to 0.5 mg mL^{-1}. After further incubation for another 24 h or 48 h, the cell viabilities to HeLa cells and HUVECs cells were determined by the conventional MTT assay. Five replicate wells were run for each concentration and each experiment was repeated three times. BMDC cells and T cells were also used for evaluation according to the same procedure as descried above. After incubation with Gd-PEG-PPy NPs for 24 h, cell viability was further determined by staining with both calcein-AM and PI, and observed using a fluorescence microscope.

In Vitro Photothermal Ablation of Cancer Cells: Photothermal cytotoxicity of the Gd-PEG-PPy NPs was evaluated with HeLa cells. HeLa cells were first seeded in 6-well plate (5×10^5 cells per well) and incubated at 37 °C in a humidified atmosphere containing 5% CO_2 for 24 h. Then the cells were incubated with Gd-PEG-PPy NPs at the concentration of 5 μg mL^{-1} for 4 h, followed by washing with phosphate buffer solution (PBS, 10×10^{-3} M, pH 7.4) and exposure to a laser diode with a wavelength of 808 nm and output power density of 1.5 W cm^{-2} for different time (0, 5, 10 min) based on our previous study.[75] After incubation for another 2 h, the HeLa cells were conventionally stained with calcein AM and PI. The fluorescence images were obtained by an inverted fluorescence microscope (Olympus, Japan) equipped with a cooled CCD camera (Keyence, Japan). For quantitative evaluation, MTT assay was further used to test the photothermal cytotoxicity of the Gd-PEG-PPy NPs. Briefly, HeLa cells were incubated in 96-well plate with density of 5×10^4 cells per well for 24 h. Then, different concentrations of Gd-PEG-PPy NPs were added and incubated for another 24 h, followed by washing with PBS (10×10^{-3} M, pH 7.4) and exposure to a laser diode with a wavelength of 808 nm and output power of 1.5 W for different time (0, 5, 10 min). Cell viabilities were determined by MTT assay after further culturing the cells for 24 h.

In Vitro and in Vivo MRI Measurement: In vitro MR imaging of Gd-PEG-PPy NPs of different concentrations were carried out on a Philips 3.0 T whole-body magnetic resonance imaging scanner (PHILIPS-14B464A) at 25 °C. The array was embedded in a phantom consisting of a tank of water to allow appropriate image acquisition. The following parameters were adopted: repetition time (TR) = 2300 ms, echo time (TE) = 15.5 ms, number of averages = 3. The relaxivity value (r_1, L mM^{-1} s^{-1}) was calculated using T_1 measurements with a series dilution of the nanoparticle dispersions in 0.9% saline. For in vivo magnetic resonance imaging, nude mice bearing U87MG tumor was used as a model. Gd-PEG-PPy NPs (100 μL, 5 mg mL^{-1}) were intravenously injected into the nude mice via the tail vein and imaged with a Bruker Pharmascan 70/16 US In vivo MRI system (TR = 1000 ms; TE = 9 ms) at different time intervals (0, 1, 18, 24 h).

In Vivo Photoacoustic Imaging: The in vivo PA imaging of Gd-PEG-PPy NPs was carried out on U87MG tumor-bearing nude mice (18–20 g). The photoacoustic signals were excited by using a Q-switched Nd:YAG laser (LS-2137/2, LOTIS TII, Minsk, Belarus) and a pumped tunable Ti:sapphire laser (LT-45 2211A, LOTIS TII, Minsk, Belarus). An unfocused ultrasonic transducer with a central frequency of 2.25 MHz was used to detect the photoacoustic signals. Before imaging, the mouse was first anesthetized and placed on a homemade shelf. Then a thin layer of ultrasonic coupling gel was coated on the tumor, followed by protruding into the water tank filled with water through a hole in the tank's bottom. PA imaging data of tumor site were collected before and after the tail intravenous injection of Gd-PEG-PPy NPs for 24 h (100 μL, 5 mg mL^{-1}).

Blood circulation and biodistribution measurement: After injection of Gd-PEG-PPy NPs into the healthy Balb/c mice (5 mg mL^{-1}, 100 μL), about 10–15 μL of blood was drawing from the mouse tail vein at different time-intervals post injection. Each blood sample was weighted and then dissolved in aqua regia. The obtained homogeneous solution was then diluted with deionized water. The concentrations of Gd^{3+} in the blood samples were measured by inductively coupled plasma mass spectrometry (ICP-MS). For biodistribution study, three female Balb/c mice bearing U87-MG tumor were sacrificed at 24 h after i.v. injection of Gd-PEG-PPy NPs (5 mg mL^{-1}, 100 μL). Major organs including heart, liver, spleen, lung, kidney, and tumor were collected, weighed, and then solubilized by aqua regia. The concentrations of Gd^{3+} in those tissue lysate samples were measured by ICP-MS. The levels of Gd-PEG-PPy NPs in blood and various organs are presented as the percentage of injected dose per gram of tissue (%ID g^{-1}).

In Vivo Photothermal Therapy: The protocol experiments were approved by the Institutional Animal Care and Use Committee at the Institute of Biophysics of Peking University. Female BALB/c athymic nude mice (5–6 weeks old) were implanted with Human glioma U87-MG cells by a subcutaneous injection of $\approx 3 \times 10^6$ cells in PBS. Treatments were started when the tumors volume reached ≈135 mm^3, which was designated as day 0. Nude mice were randomly divided into six groups (n = 8). The tumor-bearing mice were intratumorally (i.t.) or intravenously (i.v.) injected with 100 μL of 2 mg mL^{-1} or 5 mg mL^{-1} Gd-PEG-PPy NPs, respectively, and then irradiated by an optical fiber coupled 808 nm power laser diode (Hi-Tech Optoelectronics Co., Ltd. Beijing, China) at 1.5 W cm^{-2} for 10 min.[62] The other four groups including untreated mice (saline (i.t.) only), mice exposed to the laser (saline (i.t.) + laser), and Gd-PEG-PPy NPs injected (i.t. or i.v.) mice without laser irradiation were used as the controls. According to prior report,[76] an electrical temperature detector was inserted into the tumors to monitor the temperature variation during the laser irradiation. The tumor sizes were measured by a caliper at certain time interval, tumor volume was calculated as $V = (L \times W^2)\pi/6$, where L and W are the longer and shorter diameter of the tumor, respectively. In addition, mice

were sacrificed for necropsy after 20 days, major organs including heart, liver, spleen, lung, kidney, tumor tissues, or tissues at the original site of tumor were collected and fixed in formalin. Fixed tissue specimens were embedded in paraffin, stained with hematoxylin and eosin (H&E), and subsequently examined by light-field microscopy.

Supporting Information

Supporting Information is available from the Wiley Online Library or from the author.

Acknowledgements

X.L. and Y.L. contributed equally to this work. This work was financially supported by the National Natural Science Foundation for Distinguished Young Scholars (No. 81225011), State Key Program of National Natural Science of China (Grant No. 81230036), National Natural Science Foundation of China (No. 81371580 and No. 81201186), and China Postdoctoral Science Foundation (2013M530014).

Received: July 14, 2014
Revised: October 7, 2014
Published online: January 28, 2015

[1] M. P. Melancon, M. Zhou, C. Li, *Acc. Chem. Res.* **2011**, *44*, 947.
[2] K. Yang, S. Zhang, G. Zhang, X. Sun, S. T. Lee, Z. Liu, *Nano Lett.* **2010**, *10*, 3318.
[3] X. Liu, H. Tao, K. Yang, S. Zhang, S. T. Lee, Z. Liu, *Biomaterials* **2011**, *32*, 144.
[4] A. Vogel, V. Venugopalan, *Chem. Rev.* **2003**, *103*, 577.
[5] V. U. Fiedler, H.-J. Schwarzmaier, F. Eickmeyer, F. P. Müller, C. Schoepp, P. Verreet, *J . Magn. Reson. Imaging* **2001**, *13*, 729.
[6] M. K. Yu, D. Kim, I. H. Lee, J. S. So, Y. Y. Jeong, S. Jon, *Small* **2011**, *7*, 2241.
[7] C. L. Peng, Y. H. Shih, P. C. Lee, T. M. Hsieh, T. Y. Luo, M. J. Shieh, *ACS Nano* **2011**, *5*, 5594.
[8] K. Yang, L. Hu, X. Ma, S. Ye, L. Cheng, X. Shi, C. Li, Y. Li, Z. Liu, *Adv. Mater.* **2012**, *24*, 1868.
[9] E. Kim, K. Lee, Y.-M. Huh, S. Haam, *J. Mater. Chem. B* **2013**, *1*, 729.
[10] J. Kim, S. Park, J. E. Lee, S. M. Jin, J. H. Lee, I. S. Lee, I. Yang, J. S. Kim, S. K. Kim, M. H. Cho, T. Hyeon, *Angew. Chem. Int. Ed.* **2006**, *45*, 7754.
[11] S. M. Lee, Y. Song, B. J. Hong, K. W MacRenaris, D. J. Mastarone, T. V. O'Halloran, T. J. Meade, S. T. Nguyen, *Angew. Chem. Int. Ed.* **2010**, *17*, 9960.
[12] S. S. Kelkar, T. M. Reineke, *Bioconjugate Chem.* **2011**, *22*, 1879.
[13] C. Guo, Y. Jin, Z. Dai, *Bioconjugate Chem.* **2014**, *25*, 840.
[14] M. Das, R. Jain, A. K. Agrawal, K. Thanki, S. Jain, *Bioconjugate Chem.* **2014**, *25*, 501.
[15] H. Sakuma, *J. Magn. Reson. Imaging* **2007**, *26*, 3.
[16] J. L. Major, T. J. Meade, *Acc. Chem. Res.* **2009**, *42*, 893.
[17] U. I. Tromsdorf, O. T. Bruns, S. C. Salmen, U. Beisiegel, H. Weller, *Nano Lett.* **2009**, *9*, 4434.
[18] T. Lee, X. Zhang, S. Dhar, H. Faas, S. J. Lippard, A. Jasanoff, *Chem. Biol.* **2010**, *17*, 665.
[19] L. S. Boucharda, M. S. Anwar, G. L. Liu, B. Hann, Z. H. Xie, J. W. Gray, *Proc. Natl Acad. Sci. U.S.A.* **2008**, *106*, 4085.
[20] G. Stephen, G. H. Worthley, V. Fuster, Z. A. Fayad, M. Shinnar, L. A. Minkoff, *Arterioscler. Thromb. Vasc. Biol.* **2003**, *23*, 346.
[21] K. M. L. Taylor, J. S. Kim, W. J. Rieter, H. An, W. L. Lin, W. B. Lin, *J. Am. Chem. Soc.* **2008**, *130*, 2154.
[22] D. Pan, S. D. Caruthers, G. Hu, A. Senpan, M. J. Scott, P. J. Gaffney, S. A. Wickline, G. M. Lanza, *J. Am. Chem. Soc.* **2008**, *130*, 9186.
[23] X. A. Zhang, K. S. Lovejoy, A. Jasanoff, S. J. Lippard, *Proc. Natl Acad. Sci. U.S.A.* **2007**, *104*, 10780.
[24] D. Pan, S. D. Caruthers, A. Senpan, A. H. Schmieder, S. A. Wickline, G. M. Lanza, *WIRES Nanomed. Nanobi.* **2011**, *3*, 162.
[25] Z. Zhang, R. He, K. Yan, Q. N. Guo, Y. G. Lu, X. X. Wang, H. Lei, Z. Y. Li, *Bioorg. Med. Chem. Lett.* **2009**, *19*, 6675.
[26] C. W. Chen, J. S. Cohen, C. E. Myers, M. Sohn, *FEBS Lett.* **1984**, *168*, 70.
[27] S. H. Koenig, R. D. Brown 3rd, M. Spiller, *Magn. Reson. Med.* **1987**, *4*, 252.
[28] L. H. Wang, *Nat. Photonics* **2009**, *3*, 503.
[29] H. F. Zhang, K. Maslov, G. Stoica, L. V. Wang, *Nat. Biotechnol.* **2006**, *24*, 848.
[30] P. Beard, *Interface Focus* **2011**, *1*, 602.
[31] B. Cox, J. G. Laufer, S. R. Arridge, P. C. Beard, *J. Biomed. Opt.* **2012**, *17*, 061202.
[32] X. Li, X. Liang, X. Yue, J. Wang, C. Li, Z. Deng, L. Jing, L. Lin, E. Qu, S. Wang, C. Wu, H. Wu, Z. Dai, *J. Mater. Chem. B* **2014**, *2*, 217.
[33] A. Louie, *Chem. Rev.* **2010**, *110*, 3146.
[34] Y. Ma, X. Liang, S. Tong, G. Bao, Q. Ren, Z. Dai, *Adv. Funct. Mater.* **2013**, *23*, 815.
[35] Z. Zhang, L. Wang, J. Wang, X. Jiang, X. Li, Z. Hu, Y. Ji, X. Wu, C. Chen, *Adv. Mater.* **2012**, *24*, 1418.
[36] J. Chen, C. Glaus, R. Laforest, Q. Zhang, M. Yang, M. Gidding, M. J. Welch, Y. Xia, *Small* **2010**, *6*, 811.
[37] J. Chen, M. Yang, Q. Zhang, E. C. Cho, C. M. Cobley, C. Kim, C. Glaus, L. V. Wang, M. J. Welch, Y. Xia, *Adv. Funct. Mater.* **2010**, *20*, 3684.
[38] Y. Xia, W. Li, C. M. Cobley, J. Chen, X. Xia, Q. Zhang, M. E. Yang, C. Cho, P. K. Brown, *Acc. Chem. Res.* **2011**, *44*, 914.
[39] K. Yang, J. Wan, S. Zhang, B. Tian, Y. Zhang, Z. Liu, *Biomaterials* **2012**, *33*, 2206.
[40] X. Liu, H. Tao, K. Yang, S. Zhang, S. T. Lee, Z. Liu, *Biomaterials* **2011**, *32*, 144.
[41] K. Yang, S. Zhang, G. Zhang, X. Sun, S. T. Lee, Z. Liu, *Nano Lett.* **2010**, *10*, 3318.
[42] M. Zhou, R. Zhang, M. Huang, W. Lu, S. Song, M. P. Melancon, M. Tian, D. Liang, C. Li, *J. Am. Chem. Soc.* **2010**, *132*, 15351.
[43] Q. Tian, M. Tang, Y. Sun, R. Zou, Z. Chen, M. Zhu, S. Yang, J. Wang, J. Wang, J. Hu, *Adv. Mater.* **2011**, *23*, 3542.
[44] Z. Zha, S. Wang, S. Zhang, E. Qu, H. Ke, J. Wang, Z. Dai, *Nanoscale* **2013**, *5*, 3216.
[45] J. Yang, J. Choi, D. Bang, E. Kim, E. K. Lim, H. Park, J. S. Suh, K. Lee, K. H. Yoo, E. K. Kim, Y. M. Huh, S. Haam, *Angew. Chem. Int. Ed.* **2011**, *50*, 441.
[46] H. Chong, C. Nie, C. Zhu, Q. Yang, L. Liu, F. Lv, S. Wang, *Langmuir* **2012**, *28*, 2091.
[47] K. Yang, H. Xu, L. Cheng, C. Sun, J. Wang, Z. Liu, *Adv. Mater.* **2012**, *24*, 5586.
[48] Z. Zha, X. Yue, Q. Ren, Z. Dai, *Adv. Mater.* **2012**, *25*, 777.
[49] M. Chen, X. Fang, S. Tang, N. Zheng, *Chem. Commun.* **2012**, *48*. 8934.
[50] L. Cheng, K. Yang, Q. Chen, Z. Liu, *ACS Nano.* **2012**, *6*, 5605.
[51] L. Feng, C. Zhu, H. Yuan, L. Liu, F. Lv, S. Wang, *Chem. Soc. Rev.* **2013**, *42*, 6620.
[52] Z. Zha, X. Yue, Q. Ren, Z. Dai, *Adv. Mater.* **2013**, *25*, 777.
[53] Z. Zha, J. Wang, E. Qu, S. Zhang, Y. Jin, S. Wang, Z. Dai, *Sci. Rep.* **2013**, *3*, 2360.
[54] Z. Zha, Z. Deng, Y. Li, C. Li, J. Wang, S. Wang, E. Qu, Z. Dai, *Nanoscale* **2013**, *5*, 4462.
[55] J.-Y. Hong, H. Yoon, J. Jang, *Small* **2010**, *6*, 679.

[56] S. N. Goldberg, G. S. Gazelle, P. R. Mueller, *AJR Am. J. Roentgenol* **2000**, *174*, 323.
[57] P. Bourrinet, E. Martel, A. I. El Amrani, P. Champeroux, S. Richard, N. Fauchou, F. Le Coz, M. Drici, B. Bonnemain, S. Gaillard, *Invest. Radiol.* **2007**, *42*, 63.
[58] T. Ishiguchi, S. Takahashi, *Drugs R&D.* **2010**, *10*, 133.
[59] M. Sasaki, E. Shibata, Y. Kanbara, S. Ehara. *Magn. Reson. Med. Sci.* **2005**, *4*, 145.
[60] P. Caravan. *Chem. Soc. Rev.* **2006**, *35*, 512.
[61] M. N. Rhyner, A. M. Smith, X. H. Gao, H. Mao, L. L. Yang, S. M. Nie, *Nanomedicine* **2006**, *1*, 209.
[62] X. Wang, L. Yang, Z. G. Chen, D. M. Shin, *Ca-Cancer J. Clin.* **2008**, *58*, 97.
[63] S. D. Perrault, C. Walkey, T. Jennings, H. C. Fischer, W. C. Chan, *Nano Lett.* **2009**, *9*, 1909.
[64] P. A. Netti, S. Roberge, Y. Boucher, L. T. Baxter, R. K. Jain, *Microvasc. Res.* **1996**, *52*, 27.
[65] D. Pan, G. M. Lanza, S. A. Wickline, S. D. Caruthers, *Eur. J. Radiol.* **2009**, *70*, 274.
[66] J. H. Ryu, H. Koo, I. C. Sun, S. H. Yuk, K. Choi, K. Kim, I. C. Kwon, *Adv. Drug Delivery Rev.* **2012**, *64*, 1447.
[67] X. Huang, P. K. Jain, I. H. El-Sayed, M. A. El-Sayed, *Lasers Med. Sci.* **2008**, *23*, 217.
[68] P. M. George, A. W. Lyckman, D. A. Lavan, A. Hegde, Y. Leung, R. Avasare, C. Testa, P. M. Alexander, R. Langer, M. Sur, *Biomaterials* **2005**, *26*, 3511.
[69] X. Wang, X. Gu, C. Yuan, S. Chen, P. Zhang, T. Zhang, J. Yao, F. Chen, G. Chen, *J. Biomed. Mater. Res. A* **2004**, *68*, 411.
[70] A. Ramanaviciene, A. Kausaite, S. Tautkus, A. Ramanavicius, *J. Pharm. Pharmacol.* **2007**, *59*, 311.
[71] S. Jalota, S. B. Bhaduri, A. C. Tas, *Mater. Sci. Eng. C* **2008**, *28*, 129.
[72] Y. Ling, K. Wei, Y. Luo, X. Gao, S. Zhong, *Biomaterials* **2011**, *32*, 7139.
[73] L. Sampath, S. Kwon, M. A. Hall, R. E. Price, E. M. Sevick-Muraca, *Transl. Oncol.* **2010**, *3*, 307.
[74] J. A. Feshitan, F. Vlachos, S. R. Sirsi, E. E. Konofagou, M. A. Borden, *Biomaterials* **2012**, *3*, 247.
[75] L. Jing, X. Liang, Z. Deng, S. Feng, X. Li, M. Huang, C. Li, Z. Dai, *Biomaterials* **2014**, *35*, 5814.
[76] S. Wang, Z. Dai, H. Ke, E. Qu, X. Qi, K. Zhang, J. Wang, *Eur. J. Radiol.* **2014**, *83*, 117.